Adhesion and air ionization in film-based electrostatic actuation: A case study

Elie Zoghbi, Emilien Dufresne, Martino LoBue, Morgan Almanza

▶ **To cite this version:**

Elie Zoghbi, Emilien Dufresne, Martino LoBue, Morgan Almanza. Adhesion and air ionization in film-based electrostatic actuation: A case study. Sensors and Actuators A: Physical , 2026, 403, pp.117709. ⟨10.1016/j.sna.2026.117709⟩. ⟨hal-05556920⟩

HAL Id: hal-05556920

https://hal.science/hal-05556920v1

Submitted on 19 Mar 2026

HAL is a multi-disciplinary open access archive for the deposit and dissemination of scientific research documents, whether they are published or not. The documents may come from teaching and research institutions in France or abroad, or from public or private research centers.

L'archive ouverte pluridisciplinaire **HAL**, est destinée au dépôt et à la diffusion de documents scientifiques de niveau recherche, publiés ou non, émanant des établissements d'enseignement et de recherche français ou étrangers, des laboratoires publics ou privés.

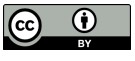

Distributed under a Creative Commons CC BY 4.0 - Attribution - International License

Adhesion and Air Ionization in Film-Based Electrostatic Actuation: A Case Study

Elie Zoghbi,[1] Emilien Dufresne,[1] Martino LoBue,[1] and Morgan Almanza[1]
Université Paris-Saclay, École Normale Supérieure Paris-Saclay, CNRS, Laboratoire SATIE, 91190 Gif-sur-Yvette, France

(Dated: 19 March 2026)

Electrostatic actuation (EA) plays an important role in applications like soft robotics and electrocaloric devices. With dielectric films, the interplay between adhesion and partial discharges plays a crucial role in the device losses and therefore represents a key challenge for optimizing the efficiency. Here, an advanced characterization method is used for measuring the position of the film during the actuation as a function of the applied voltage using, as a probe, the injection of a high-frequency voltage and the entailed capacitive response. This highly sensitive measurement of the film position during the actuation cycle reveals, on the one hand, the presence of a minimum voltage required for triggering the EA, and on the other, the appearance of charges on the film surface modifying the electrostatic force when the voltage exceeds a given threshold. The presence of surface charges is confirmed by fitting the electrostatic force and by current measurements before and after they appear. The study provides a new insight for discussing the fundamental trade-off between a lower working voltage bound defined by film adhesion, and an upper one imposed by the ionization of air, a very general issue all the EA devices will have to tackle in order to optimize their efficiency. As a case study, we analyze the losses on a zipping film-based electrostatic actuator using an 8 μm thick Polypropylene film as the moving part.

Keywords: Electrostatic actuation, dielectric films, losses, film adhesion, air ionization

1. Introduction

Electrostatic actuation (EA) is used in microelectromechanical systems (MEMS), soft actuators[1,2], thermal switches[3], as well as electrocaloric cooling systems[4–6] due to its scalability and fast response. The working principle of the EA is based on Coulomb's law: applying a voltage across two electrodes with a dielectric between them causes opposite charges and electrodes to attract. In the EA, one of the two electrodes is fixed while the other is movable. The EA generally has three main architectures[7,8]: the comb drive actuator, the parallel plate, and the curved electrode zipping actuator. In this paper, the zipping configuration, illustrated in Fig. 1, is used because of its higher force and larger displacement at lower voltage compared to the other configurations[7]. In this configuration, the movement of the film from one electrode to the other takes place as a transversal displacement of an S-shaped fold, as shown in Fig. 1. When the upward voltage V^u equals the trigger voltage V_{tr} and the downward voltage V^d is 0 V, the film moves up (the S-fold moving towards the left in the figure). Conversely, when the voltages are reversed, the film moves down (the fold goes back to the right).

Electrostatic zipping actuators have been studied for several decades, mainly for MEMS and soft robotic applications[9]. The emergence of highly promising electrocaloric coolers has revived interest in S-shaped zipping actuators, a key component for thermal switches[3,5]. Consequently, loss analysis and minimization—hitherto rather neglected topics—have become key challenges for thermal management and energy conversion applications. Indeed, minimizing losses in the zipping actuator is essential to achieve high cooling efficiency.

Previous studies have been focused on viscous losses[10,11], an approach rather similar to the squeeze film damping analysis for a parallel plate configuration. Although these investigations properly describe the dynamic losses in the EA, they neglect static losses related to adhesion, the triboelectric effect, and other mechanisms. Nonetheless, when using the EA between two films, adhesion forces/energy involving different mechanisms, such as Van Der Walls forces, capillary force[12,13] or interdiffusion force[14] appear, and can play a rather relevant role indeed. In standard conditions, at a relative humidity of 50% and with an air gap of 100 nm, Van Der Waals and capillary forces[12,13] produce 1 Pa and 10 kPa pressures, with surface energies of 3.5 and 14.4 μJ/cm^2, respectively.

On the other hand, charges trapped on the dielectric layer and coming from the triboelectric effect or conduction create a distortion of the electrostatic force[15]. In the case of the triboelectric effect, the charge density is -27.23 μCm^{-2} for Polypropylene, which is a rather small value compared to other materials[16]. Furthermore, when the voltage is increased to enhance the force, a high electric field (with possible field concentration on the electrode protuberance associated with the surface roughness) allows a complex charge displacement/leakage current mechanism through air ionization or charge emission[17,18]. For instance, in the case of electrocaloric zipping-based devices using voltage above 800 V for actuation[4,5], a partial discharge is expected, a shortcoming that has been hardly mentioned so far.

A real-time knowledge of the displacement (i.e., position, velocity) of the film all along the actuation cycle is a prerequisite for studying forces/losses within an EA device in order to single-out the mechanisms that hamper the displacement. Getting such knowledge is a difficult task with films of typical thickness below 10 μm, and with actuation times of the order of 10 ms. In this paper, an original method inspired by the AC voltammetry[19] in electrochemistry is used to measure the position of the film during the actuation in actual working conditions. This involves injecting high-frequency excitation in order to estimate the film's capacitance and deduce its po-

sition.

The paper is organized as follows. In the experimental setup section, we describe the architecture of the three-film-based electrostatic actuator. The position-sensing method is used to precisely describe the motion and to study the effect of different parameters, such as the zipping fold angle and the voltage profile. It gives us the opportunity to discuss the losses and the time of actuation, two keys parameters for application purposes. The setup is tested on a zipping EA device using an 8 μm thick Polypropylene film as the moving part. The minimum voltage needed to overcome the adhesion forces and its impact on the EA losses are studied in detail. Furthermore, the tradeoff between high voltage advantages (i.e., overcoming adhesion, fast switching) and shortcomings associated with the appearance of surface charges on the films is discussed. The original sensing method used allows an unprecedented insight into the way surface charges modify the electrostatic force, modifying the EA functioning. In the conclusions, some general strategies to optimize EA are discussed.

2. Experimental setup

2.1. Architecture studied

The device presented here is composed of three films: an upper one, a middle one with an S-shape fold, and a bottom one. A schematic of the device is shown in Fig. 1. Each film is composed of a dielectric (green layer in Fig. 1) and an electrode (black line in Fig. 1). The upper and lower film voltages are V^u and V^d, respectively. The middle film with the S-shape is kept at GND. Gray silicone supports (8 mm of Sylgard 184) are used to constrain the S-shape fold, and blue clamps are used to hold the films in position within the device and secure the overall assembly. All the films have a surface of 3.8×0.9 cm^2. In this study, Polypropylene (PP) dielectric films and Aluminum (Al) electrodes have been used. Both materials exhibit typical properties, allowing the results discussed here to serve as general guidance for optimizing zipping actuators, regardless of the specific materials employed. PP is a common and well-known dielectric material, making it a representative starting point for identifying and understanding the physical mechanisms involved in the actuator. In this study, we used a commercially available pre-fabricated roll of PP capacitor film, consisting of an 8 µm thick PP layer coated with an 8 nm thick Al layer deposited by sputtering. A 2 mm stripe of Al is removed from the edges of the middle film in order to avoid electrical shortcuts.

The variations of the electrostatic pressure (i.e., the small red arrows in Fig. 1) due to the voltage are at the origin of the force driving the movement of the fold, the very essence of the zipping actuation. Trapezoidal voltages are imposed on V^d and V^u, and whenever the voltage of one electrode is non-vanishing, the other is zero in order to avoid overlapping. The middle film moves down when V^d increases and moves up when V^u increases.

As shown in Fig. 2, the trapezoidal voltage is defined by three parameters, namely the rising time τ_r, the maximum voltage V_{max}, and the period τ_p. The voltage is applied using a voltage amplifier (HA2B5S from HiVolt) through a *RLC* filter to attenuate the amplifier noise (R =320 Ω, L =0.2 mH, and C =10 μC). The signals to drive the amplifier are generated by an acquisition card (NI USB-6453). At the same time, the voltage and current in the films are accurately measured using a voltage divider (1/100 ratio) and using a current amplifier (AD8228 from Analog Devices), both connected to an acquisition card (Dewesoft Sirius XHS).

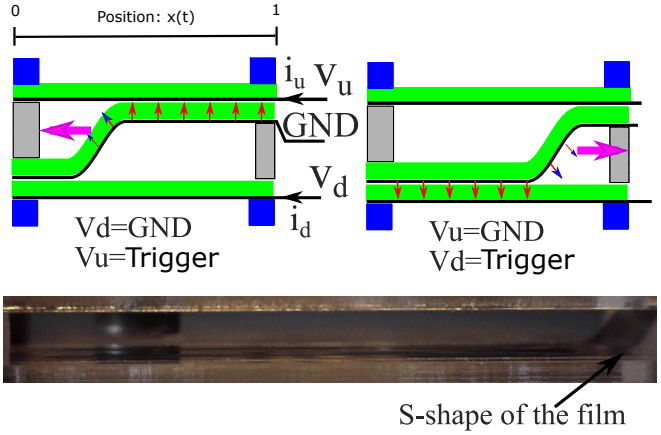

FIG. 1. Schematic of the zipping-based actuator in two configurations: on the left, the contact with the upper film, and on the right, the contact with the bottom film. The picture at the bottom shows the right configuration.

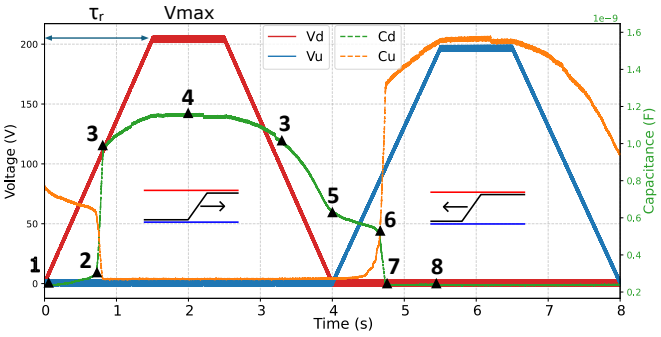

FIG. 2. Trapezoidal voltage (V^d, V^u) and capacitance profiles (C_d, C_u) with the definition of the rising time τ_r and the maximum voltage V_{max}. The steps of the EA motion (1 to 8) are defined in Fig. 3.

2.2. Position-sensing method

Within the described architecture, in addition to their respective voltages V^d and V^u, the two electrodes are associated with two capacitors, C_d and C_u (Eq. (1) and (2)), describing the dielectric film jointly with the air gap. The capacitance C_d (C_u) formed by the bottom (upper) and middle films is the sum of three terms: one that depends on the area in contact with the bottom (upper) electrode, xA, another that depends

on the part of the middle film still in contact with the upper (bottom) electrode $(1-x)A$, and a constant term that corresponds to the static part of the film (planar model):

$$C_d = \varepsilon_0 \varepsilon_r A \left[\frac{x}{d + e_d \varepsilon_r} + \frac{1-x}{d + e\varepsilon_r} \right] + C_0, \quad (1)$$

$$C_u = \varepsilon_0 \varepsilon_r A \left[\frac{1-x}{d + e_u \varepsilon_r} + \frac{x}{d + e\varepsilon_r} \right] + C_0, \quad (2)$$

where $A = 3.8 \times 0.9$ cm^2 is the maximum surface of contact (i.e., the total film surface), ε_r is the relative permittivity of PP (~ 2.8), x is the fraction of the film which is in contact with the bottom as shown schematically in Fig. 1, and C_0 is the capacitance associated with the static part of the film. As a first approximation, the area corresponding to the S-shape fold is neglected (i.e., the fold is assumed to be vertical). When the films are in contact at the bottom (upper) part, the electrodes are separated by a layer of dielectric of thickness d, and by a very thin air layer of thickness e_d (e_u). The latter is a parameter mimicking the quality of the contact (i.e., residual air, surface roughness, dust, and impurities on the film surfaces, etc.). When the middle film is not in contact, the electrodes are separated by the superposition of a thick air layer and a PP layer with thicknesses of e and d, respectively. The air gap is three orders of magnitude larger than the thickness of PP, i.e, $e \gg d$. This makes the capacitance related to the PP alone dominate the one where the air layer has to be taken into account. Eq. (1) shows that C_d is a function of x and e_d, and Eq. (2) shows that C_u is a function of $(1-x)$ and e_u. Therefore, when an increase in C_d is accompanied by a decrease in C_u, and vice versa, this is directly related to a change of x, namely to the position of the S-fold. Conversely, a variation of one capacitance only, C_d or C_u, is related to a change of e_d or e_u, respectively. This makes the direct measurement of the two capacitances during the actuation cycle a tool for real-time probing of the fold position, and of the quality of the contact, offering a unique insight into the functioning of the actuator.

The position-sensing method consists of adding a small high-frequency sinusoidal excitation voltage (i.e, 1 V amplitude at a frequency of 1 kHz) to the trapezoidal voltage, and deducing the capacitance value from the measured current as shown in Fig. 2 and 3. Each capacitance value is an average over a 10 ms time (or 1 ms when $\tau_r = 5$ ms), and the reported capacitances are not averaged over an actuation cycle. The waveforms overlap precisely over successive cycles, confirming the high reproducibility of the actuation mechanism. The capacitance measurements were validated by measuring a reference capacitor with a known value (2.005 nF). The impedance measured at 1 kHz also corresponds to a capacitance, as indicated by the 90° phase lag between the current and the voltage.

Fig. 3 shows the plot of C_d and C_u measured along a working cycle as a function of the difference between the electrodes voltages $\Delta V = |V^d| - |V^u|$. Absolute values are used in order to keep the same orientation even when a negative voltage will be used in the following part. In a reversible actuation cycle, a unique correspondence between voltage and capacitance (i.e, position of the film) would be expected. The hysteretic behavior apparent in Fig. 3 is a signature of the presence of dissipation. The minimum force/voltage needed for starting the EA motion is the trigger voltage V_{tr}. The trigger voltage is a crucial parameter for the EA.

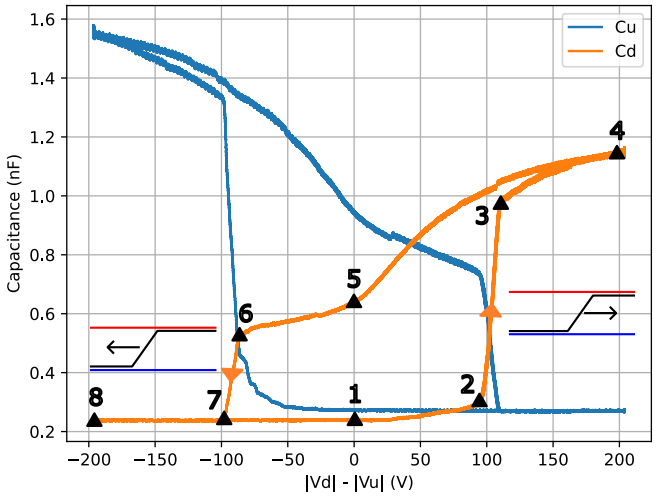

FIG. 3. Capacitances C_d and C_u as a function of $\Delta V = |V^d| - |V^u|$. Steps 1–8 of the EA motion are annotated on the C_d curve.

The hysteresis cycle shown in Fig. 3 can be used for carrying out a detailed analysis of the different steps of the actuation cycle thanks to the knowledge of the position of the film. We shall use as reference the points marked with numbers from 1 to 8 for C_d in Fig. 3. In 1, where $\Delta V = 0$, the middle film is fully in contact with the upper electrode. Increasing ΔV, the film hardly moves till point 2, where it quite suddenly loses contact with the upper electrode. The value of ΔV at 2 is the so-called trigger voltage V_{tr}. The steep increase of C_d between the points 2 and 3 associated with a similar decrease of C_u corresponds to the movement of the S-shape fold from left to right, and to the entailed displacement of the middle film from the upper to the bottom electrode. In 3, the film is fully in contact with the bottom electrode. The further increase of ΔV up to the point 4 slightly modifies C_d but does not change C_u. This is due to the increased electrostatic pressure promoting the contact and reducing e_d. This part of the cycle, where the surface of the middle film is in full contact with one of the two electrodes, and the S-shape fold doesn't move, is mostly reversible as C_d follows almost the same trajectory back and forth from 3 to 4, as well as from 4 to 5. This shows the elastic nature of the forces involved in the contact. When the electrostatic force of the bottom electrode drops to zero, the film stays in contact with the bottom side in 5. Between the points 5 and 6, $V^d = 0$ while V^u starts to increase, reversing the direction of the electrostatic force towards the upper film.

At first, C_d slightly decreases while C_u remains constant. This indicates a reduction in the quality of the contact between the middle and the bottom film. When reaching $\Delta V = -50$ V,

the capacitance C_u starts to increase, indicating an improvement of the contact with the opposite side (i.e., a decrease of e_u). Between 6 and 7, the middle film is moving towards the upper film as shown by the simultaneous variation of C_d and C_u. From 7 to 8, the middle film is already fully in contact with the upper film, and the capacitance C_d is low, but C_u continues to slightly increase due to the decrease of e_u. Finally, at 8, the maximum voltage is reached for V^u, and the configuration of C_d and C_u is now reversed. Henceforth, the mechanism taking place between 7 and 1 is akin to the one described for the 3 to 5 part.

The bottom and top capacitance maximum values are 1.18 and 1.58 nF, respectively. This, in terms of the air-layer picture, corresponds to a thickness difference $e_d - e_u \approx 0.8\ \mu$m. The order of magnitude below the micrometer range reaches the very limits of the air-layer thickness model for mimicking the contact between the surfaces. As a matter of fact, the quality of the contact is very possibly strongly affected by the deposition upon the films of the dust present in the air. Indeed, more abundant deposition of dust on the bottom film, due to gravity, can explain why C_u is higher than C_d.

In summary, the key parameters of this hysteresis cycle are the down and up trigger voltages, V_{tr}^d (down) and V_{tr}^u (up), respectively, for steps 2 and 6. The triggers also define the hysteresis cycle width. The capacitance versus voltage plot gives a detailed representation of the film motion, and its hysteresis is related to actuation losses that can be computed from the integration of the $C(V)VdV$ cycle as shown in Fig. 4.

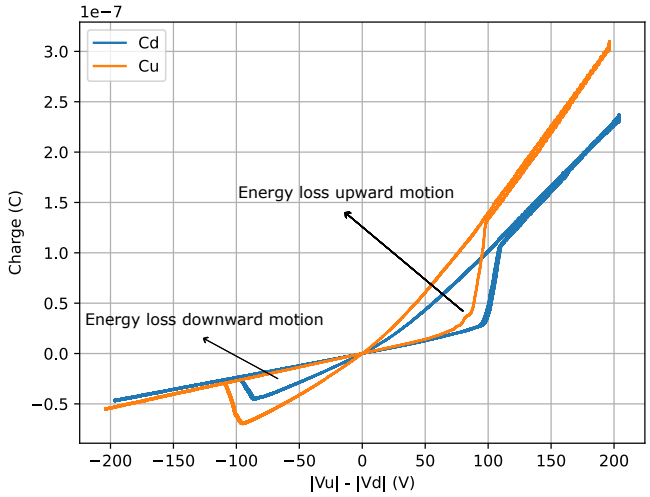

FIG. 4. Charge versus the voltage, with the area in the four triangles being the energy loss of one EA cycle.

3. Results and discussion

3.1. Effect of the fold angle

The previous section relied on a simplified representation of the S-fold, where the latter was considered perpendicular to the film surfaces. Here, we shall relax this crude simplification and study the role of the fold shape, namely the effect that different fold angles have on the actuation cycle. The angle of the S-shape fold section of the middle film is adjusted and measured through video recording (Dino-lite camera). The fold angle is governed by the distance between the film clamped boundaries, and the actual length of the film. Fig. 5 shows that the trigger voltage is proportional to the angle of the film. This suggests that reducing the angle can increase the actuation efficiency. A thin-film peeling model that includes the elastic term[20], and the electrostatic force computed from the finite element method, is unable to reproduce the linear trend observed in our measurements. As the model neglects the role of film bending[20], we can infer that the latter represents a key energy term in explaining the trigger voltage reduction observed at lower angles. As all the features discussed in what follows, but the trigger voltage, are independent of the S-fold angle, we shall use an angle of 42° corresponding to the value spontaneously resulting from device fabrication. Similarly, all the results are carried out under the same ambient experimental conditions with a temperature between 20 and 24 degrees Celsius, a relative humidity between 40 and 50 %, and at atmospheric pressure.

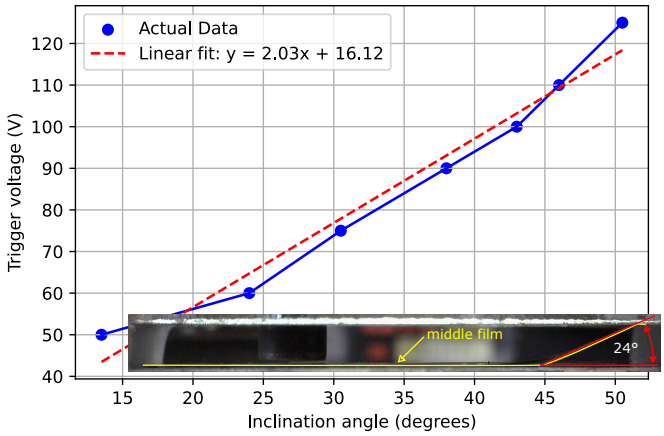

FIG. 5. Trigger voltage as a function of the S-shape fold inclination angle as defined in the bottom picture.

3.2. Analysis of different actuation regimes

Here we shall discuss the way the rising time of the voltage, τ_r, as defined in Fig. 2, and the actuation time τ_{EA}, the time the film need for fully changing contact from one electrode to the other (i.e, the duration of a complete sweep of the S-fold from one side to the other) define the regime of the actuation. Indeed, the competition between these two characteristic times defines the type of regime leading the actuation process. This can be explained in the following way. Let us assume that the driving force of the S-fold movement is the difference between the electrostatic force and the air viscous force. Our measurements show that, when the movement starts at V_{tr}, the terminal velocity v_t is reached in less than 1 ms. From this standpoint, we can define three actuation regimes:

1. the *quasi-static regime*: when $\tau_{EA} \ll \tau_r$, the film movement takes place at nearly constant voltage, V_{tr}, and thence it is driven by a constant force $F_e(V_{tr})$. In this regime, the film moves at constant velocity $v = v_t(F_e(V_{tr}))$;

2. the *field-motion coupled regime*: $\tau_{EA} \approx \tau_r$. Within this regime, the voltage is changing during the film movement. In this case, the driving force, and therefore the terminal velocity, are not constant during the actuation, and the S-fold shows an accelerated motion where $\dot{v}$ is a function of $\dot{V}$;

3. the *dynamic regime*: when $\tau_{EA} \gg \tau_r$ the film movement takes place mostly at $V = V_{max}$. This makes the motion velocity constant, with $v = v_t(F_e(V_{max}))$;

The three regimes, as they are defined above, are easily detected in Fig. 6 where a set of cycles performed at different τ_r, and constant V_{max} are shown. The outer loop (black line), performed at $\tau_r = 5$ ms, shows an abrupt vertical increase (decrease) in the capacitance associated with the film movement taking place at constant voltage, $V = V_{max}$. This loop corresponds to the above-defined dynamic regime. The inner loops, performed at increasing values of τ_r, show an increase (decrease) in the capacitance taking place with a slight positive slope. Nonetheless, as apparent in Fig. 6, the mentioned slope increases as τ_r becomes longer, reaching a nearly vertical capacitance change at $\tau_r = 450$ ms. This shows that the limit for $\tau_r \to \infty$ would be another square hysteresis cycle, corresponding to the quasi-static regime where the film displacement takes place at constant voltage V_{tr}.

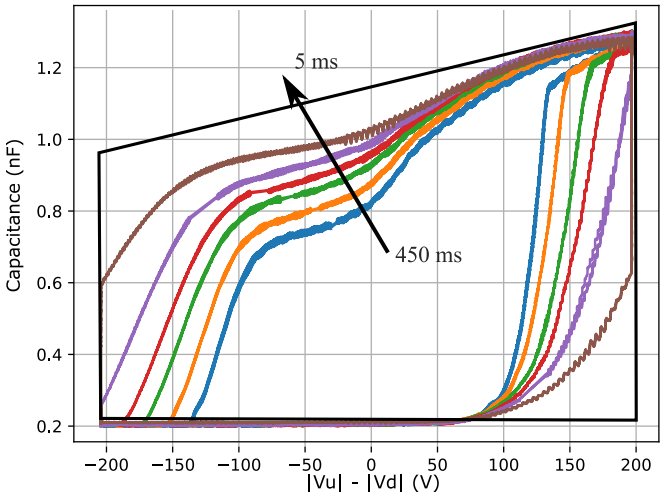

FIG. 6. Capacitance C_u as a function of $|V^u| - |V^d|$ for different rising times, $\tau_r = 450, 300, 200, 150, 100, 50, 5$ ms.

In terms of energy loss, for the back and forth movement of the EA, and for the quasi-static cycle (τ_r = 1.5 s), which represents the lower limit, we have 3.25 μJ/cm^2. For comparison, capillary force losses[13] show an upper limit of 14.4 μJ/cm^2 as a surface energy, and Van der Waals forces[21] have a surface energy of 3.5 μJ/cm^2 for non-polar molecules like Polypropylene. Although a comparison would require detailed knowledge of the quality of the contact, the orders of magnitude are rather similar, showing that the role of these forces in the adhesion mechanism cannot be ruled out. For the field and motion coupled cycle (τ_r = 50 ms) and the dynamic cycle (τ_r = 5 ms), the loss goes up to 24 and 27.7 μJ/cm^2 respectively, being nearly eight times greater than in the quasi-static regime. This shows the increasing relevance of dynamic losses ($\sim \Delta C\, V_{max}^2$) when the actuation speed is increased. To achieve faster actuation and reduce the actuation time τ_{EA}, V_{max} can also be increased, as shown in Fig. 7. However, this comes at the cost of a quadratic increase in losses as a function of the maximum voltage. Considering the Poiseuille flow model proposed in our previous work[10], the viscous energy loss per unit surface area is estimated to be near 2.2 μJ/cm^2 in the dynamic cycle (τ_{EA} = 25 ms), accounting for 9 % of the losses measured, indicating more complex dynamic loss mechanisms.

In addition, Fig. 7 shows a change of slope of the linear dependence of $\tau_{EA}(V_{max})$ taking place at $V_{max} \approx 300$ V. This is the signature of some new physical mechanism leading the film movement within the dynamic regime driven by high voltages. This will be the object of the next section.

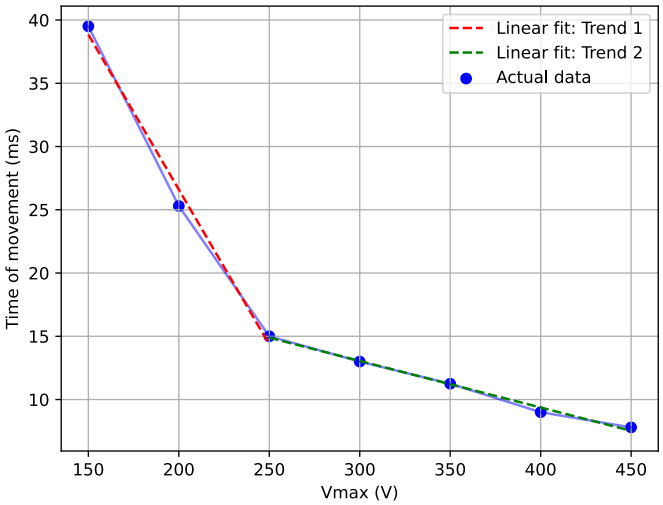

FIG. 7. Time of movement of the EA τ_{EA} (up to down contact) against the maximum voltage in the dynamic cycle ($\tau_r = 5$ ms). The τ_{EA} is calculated between steps 2 and 3 in Fig. 2, a region where the speed is constant.

3.3. Effect of the surface charge on the force

Here we shall study the role of surface charges, appearing at high voltage due to air ionization, as a candidate for explaining the two-slope regime apparent from Fig. 7.

The study of the appearance of charge on the dielectric has been carried out in three steps. First, quasi-static cycles have been measured at $\pm$ 200 V, to use them as a reference. Second, a dynamic cycle at 450 V was applied to transfer the charge on the dielectric. This step, a rather typical actuator working cy-

cle, has been performed with a positive applied voltage in order to always get the very same charge polarity. Lastly, quasi-static cycles at $\pm$ 200 V are used again to measure changes in the force due to the appearance of charge on the dielectric.

Quasi-static cycles before and after the dynamic cycle are shown in Fig. 8 and 9 for a positive and a negative driving voltage, respectively. In Fig. 8, with 200 V, we notice a widening of the hysteresis, while in Fig. 9, with -200 V, the hysteresis cycle gets narrower. Hysteresis is plotted as a function of the difference between the absolute values of the bottom, and top voltages, $|V^d| - |V^u|$, in order to show curves measured when the force drives the film down ($|V^d| - |V^u| > 0$), and up ($|V^d| - |V^u| < 0$) together. Cycles measured before, and after the 450 V training, differ in wideness due to a change of V^d_{tr} and V^u_{tr}. In what follows, we shall show that this behavior is related to the change in the electrostatic force due to the presence of additional charges on both sides, as schematically shown in Fig. 10 (a), where the transfer of charges occurs from the electrode (black) to the dielectric layer (green). Such charge transfer is mainly due to the ionization of air. The polarity of the charges, as illustrated in Fig. 10 (a), is determined by the polarity of the applied voltage during the $V_{max} = 450$ V cycle. As the middle film is kept to GND, the surface charges σ_d and σ_u on the bottom and the middle films, respectively, have opposite polarity. The effect of charges is apparent in Fig. 8, where V^d_{tr} increases from 90 V to nearly 140 V after cycling at 450 V. Similarly, V^u_{tr} is around 130 V before the 450 V cycling and rises to 180 V afterwards. The effect is different in Fig. 9.

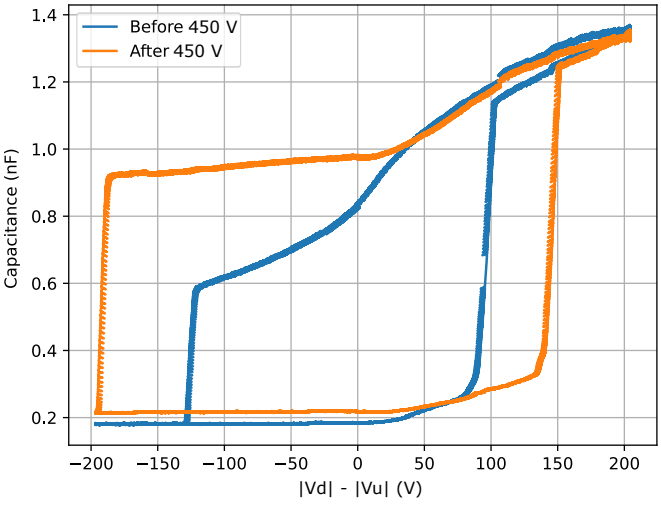

FIG. 8. Capacitance C_d in the quasi-static cycle at $V_{max} = +200\ V$ before and after the dynamic cycle at 450 V.

In what follows, we shall propose a model for describing the way surface charges modify the electrostatic force during the actuation. The model describes the electrostatic force between three parallel, rigid films, with the top and bottom at V^u and V^d, respectively, and the middle grounded. The S-fold is modelled by dividing it into two parts along an effective area, with each part in contact with one side, as schematized by the dashed pink box in Fig. 10 (b-c). After this simplification, the

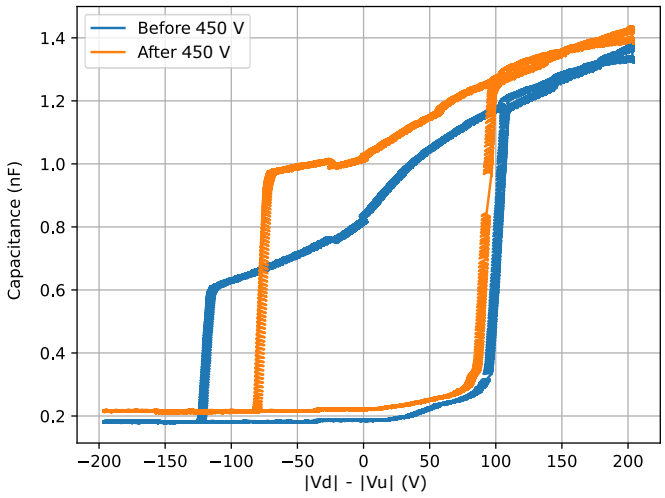

FIG. 9. Capacitance C_d in the quasi-static cycle at $V_{max} = -200\ V$ before and after the dynamic cycle at 450 V.

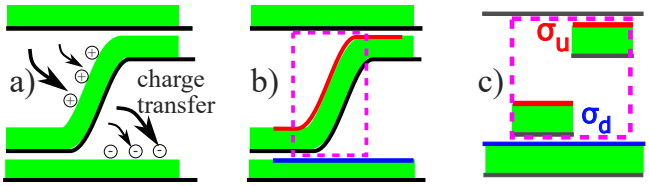

FIG. 10. a) Schematic of the charge transfer, b) appearance of charges on the dielectric and the system where electrostatic forces are computed (dashed box), c) parallel plate model used to estimate the resulting forces.

electrostatic force is defined through the introduction of two effective voltages taking into account the electric field reduction due to the surface charges present on the top, σ_u, and bottom, σ_d, films. In this way, we define two effective voltages, $V^u_{eff} = V^u - V^u_{\sigma_u}$ and $V^d_{eff} = V^d + V^d_{\sigma_d}$, where $V^u_{\sigma_u}$ ($V^d_{\sigma_d}$) are the competing voltage offset terms depending on the charge density present on the top surface of the middle (bottom) film. They write:

$$V^u_{\sigma_u} = \frac{\sigma_u d}{\varepsilon_0 \varepsilon_r}, \tag{3}$$

$$V^d_{\sigma_d} = \frac{\sigma_d d}{\varepsilon_0 \varepsilon_r}, \tag{4}$$

where d is the thickness of the film. Thence, the electrostatic pressure oriented downward is:

$$P_e(V^u_{eff}, V^d_{eff}) = \frac{\varepsilon_0 \varepsilon_r^2}{2d^2}\left[(V^d_{eff})^2 - (V^u_{eff})^2\right]. \tag{5}$$

It is worth noting that, as long as the sign of V_{max} is not reversed, the charges on the film surfaces that appear after application of $V_{max} = 450$ V reduce the electric field, and so the effective voltage. On the contrary, reversing V_{max}, the surface charges amplify the actuating electrostatic field and reduce the trigger voltage.

Eq. (5) is used to extrapolate the electrostatic pressure corresponding to the trigger voltage measured on the quasi-static cycle in the absence of surface charges. Indeed, taking advantage of the fact that when $\sigma_u = \sigma_d = 0$, $V^u = V^u_{eff}$, and $V^d = V^d_{eff}$, the pressure corresponding to the trigger voltage in the absence of charges can be calculated using Eq. (5). Thence, the two trigger pressures, $P^u_{tr} = P_e(V^u_{tr}, 0)$, and $P^d_{tr} = P_e(0, V^d_{tr})$ can be estimated. In Fig. 11, the plot of P_e from Eq. (5), when no surface charges are present, is shown (black line). The two black points show the values of P^u_{tr} and P^d_{tr}. Now, considering that there are no reasons for the trigger pressure to be affected by the presence of charges, the two values worked out from the measurements performed in the charge-less case can be used to fit the P_e curve after cycling at 450 V, keeping the same V_{max} (blue line) when the surface charges compete with the applied voltage, and reversing the sign of V_{max} (red line) when the surface charges amplify the applied voltage. In this way, the electrostatic pressure model allows us to work out, using expressions (3) and (4), a first estimation of the surface charge densities σ_u and σ_d induced when cycling up to $V_{max} = 450$ V. From $P_e(V^u_{eff}, V^d_{eff})$, we get $V^u_{\sigma_u} = 50$ V and $V^d_{\sigma_d} = -30$ V, corresponding to $\sigma_u = 155\ \mu\mathrm{C\,m^{-2}}$ and $\sigma_d = -94\ \mu\mathrm{C\,m^{-2}}$, respectively.

Besides, it is worth noting that the force resulting from the charge transfer (with $V_{max} > 450$ V) can be used to keep the film in motion without any applied voltage, making it possible to obtain an alternative motion using a single voltage source.

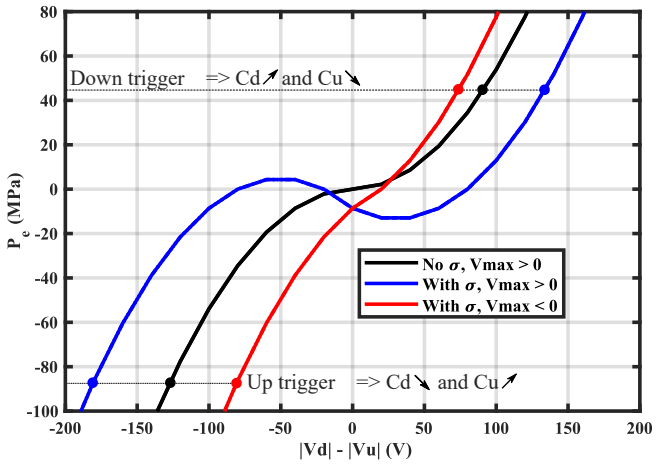

FIG. 11. Electrostatic pressure without or with charge ($V^u_{\sigma_u} = 50$ V and $V^d_{\sigma_d} = -30$ V) and with $\pm$ 200 V.

3.4. Effect of the surface charge on the current

To cross-check the surface charge estimation given in the previous section through a rather strong assumption on their role as the main cause of the electrostatic force reduction, we use the direct measurement of the current resulting from the displacement of the charged film for probing σ_u and σ_d. From Eq. (1) and (2), considering that $e \gg d$, the current can be worked out through the following expressions:

$$i_d = \frac{d}{dt}\left[xA\frac{\varepsilon_0\varepsilon_r(V^d + V^d_{\sigma_d})}{d} + C_{du}V^u\right], \tag{6}$$

$$i_u = \frac{d}{dt}\left[(1-x)A\frac{\varepsilon_0\varepsilon_r(V^u - V^u_{\sigma_u})}{d} + C_{du}V^d\right], \tag{7}$$

where C_{du} is a parasitic capacitive coupling between the top and bottom electrodes, and A is the above-defined total film surface. The method to estimate the bottom surface charge density is presented in detail, and the same approach has been used for the upper film.

The current i_d results from the voltage variations or from the film displacement as described by Eq. (6). The current i_d resulting from movement and occurring at $V^d = 0$ but with an effective voltage $(V^u - V^u_{\sigma_u}) \neq 0$, is directly related to σ_d. In order to avoid noise from the voltage amplifier and achieve sufficient sensitivity, the bottom film is short-circuited via a current amplifier (SR-570 with a 1 μA/V sensitivity, a low-pass 12 dB filter with 10 kHz filter frequency, and a low noise gain mode) to get a reliable measurement.

The current i_d measured during the film displacement induced by the application of the upper voltage V^u is shown in Fig. 12. Two different phases are apparent. In phase 1, the voltage V^u (blue curve) rises rapidly ($\tau_r = 5$ ms) while the film is still not moving (i.e., $x(t)$ is constant). The resulting current depends on $C_{du}\frac{dV^u}{dt}$ only, regardless of the presence of surface charge. In phase 2, under constant voltage, the film moves such that x goes from 1 to 0. During this second phase, the measured current is directly related to the presence of surface charges (i.e., to $V^d_{\sigma_d} \neq 0$). The green line in Fig. 12, and 13 shows the current measured before the high voltage cycling (i.e., in the absence of surface charges). The difference with the red line, showing the current measured after 450 V cycling, confirms the presence of non-vanishing σ_d, and σ_u. The fluctuation in the current signal is possibly related to the surface charge heterogeneity[22].

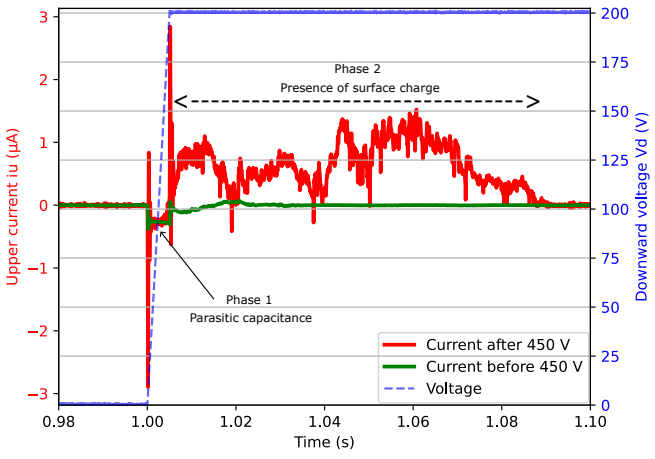

FIG. 13. Upper current i_u before and after 450 V dynamic cycling, with $V^u = 0$ and the bottom upper voltage V^d that drives the downward film movement.

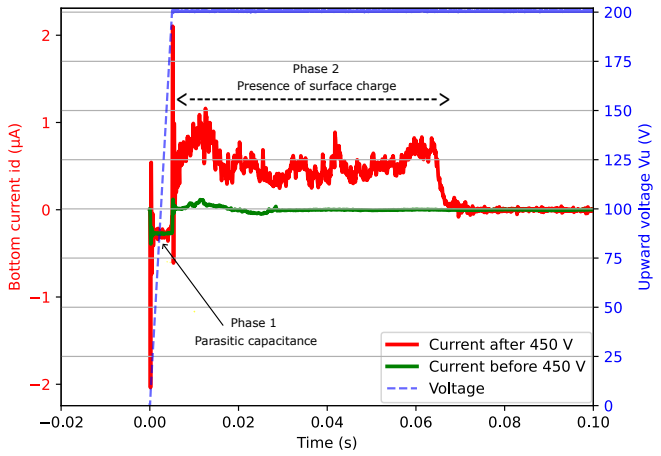

FIG. 12. Bottom current i_d before and after 450 V dynamic cycling, with $V^d = 0$ and the upper voltage V^u that drives the upward film movement.

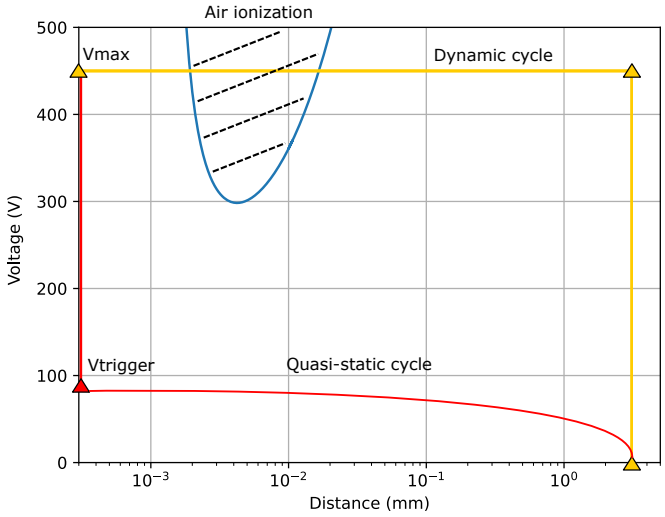

FIG. 14. Paschen curve in blue for the air at a pressure of 1 Bar, and two paths going from 0 V to V_{max} in yellow and in red, with a rising time τ_r of 5 ms and 1.5 s respectively. The area with black dashed lines represents the region where air ionization occurs.

Surface charges are directly calculated from the measured currents through the integration of Eq. (6) and (7). For the bottom current, we get a positive charge of $q_d = 1$ nC before the 450 V cycling, and a negative one $q_d = -31$ nC afterwards. The latter corresponds to an offset voltage $V^d_{\sigma_d} = -29$ V. For the top current, the charge has a value of $q_u = -2$ nC before 450 V, and a value of $q_u = 54$ nC afterwards. This corresponds to an offset voltage of $V^u_{\sigma_u} = 51$ V. While the initial charges measured are possibly related to the triboelectric charge[16], or the edge effect of the model (capacitors), the charges obtained after 450 V are in good agreement with the offset voltages estimated with the electrostatic pressure model, in the previous section (-30 V and 50 V). This confirms the leading role of surface charges in modifying the electrostatic force.

The slight difference between the top and bottom charges $|q_u| > |q_d|$ can be due to several effects, such as small variations in the electric field, slight shifts in the electrode position, fluctuations of the contact quality, as well as differences between ion and electron mobility.

3.5. Partial discharge and air ionization

The Paschen curve describes the breakdown voltage of a gas as a function of the product of its pressure and the electrode distance. The blue curve in Fig. 14 shows a typical breakdown threshold. The threshold value can depend on many features, such as the air temperature, the relative humidity, the geometry of the electrodes, etc.[23–25]. Besides, when the gap gets below 4 μm, the quantum tunnelling of electrons must be taken into account, inducing electric field enhancement at microprotrusions (i.e, material roughness) and modifying the work function of the electrode material[26,27].

In the case studied here, jointly with the two conductors, and the air gap, a dielectric layer that blocks the charges is present. In this case, the partial discharge in the air is ignited when the voltage overcomes the Paschen curve. As soon as enough charges are deposited on the dielectric, the voltage/electric field in the air, related to the effective voltage, is reduced, and the avalanche extinguishes. Thence, the appearance of charges depends on the voltage and on the rising time as described by the two trajectories in Fig. 14. The red path represents the case where the voltage change is slow, and the film motion occurs at V_{tr}, the above-defined quasi-static regime. As a result, air ionization does not occur during the film displacement, as apparent by the fact that the red path doesn't cross the air ionization region (the area with black dashed lines). However, in the yellow path (dynamic cycle), where the voltage change is fast, the motion occurs at V_{max}. When V_{max} is above the air ionization threshold, the yellow path gets through the air ionization region, and surface charges appear. Then, the deposited charge reduces the effective voltage below the ionization threshold and limits the electrostatic force. This explains the two regimes apparent in Fig. 7 where the change of slope takes place near 300 V, close enough to a typical Paschen discharge threshold.

4. Conclusion

In this work, we use the position-sensing method to study the actuation losses of a typical electrostatic actuator functioning with the zipping configuration. The experimental setup used here allows direct measurement of the position of the actuator's moving film as a function of the applied voltage and time. In this way, it has been possible to single out three actuation regimes. The study focuses on the two extreme ones, namely the quasi-static and the dynamic ones. The former shows rate-independent features allowing to define the static actuation losses and the key parameter characterizing them, namely the voltage trigger V_{tr}. The latter shows strong rate dependence and is used to study the reduction of efficiency

taking place when high voltages are used to increase the actuation speed.

Furthermore, the main physical mechanisms underlying static and dynamic losses are studied and discussed. Dynamic losses include electrical and viscous contributions. The static losses primarily arise from adhesion forces between the middle film and the two other films. Thanks to the capacitive method used here, the role of the quality of the contact between films under the effect of the electrostatic pressure is discussed in detail. Besides, the study of the quasi-static hysteresis loops points to capillary adhesion and van der Waals forces as the main factors responsible for the mechanisms hindering the actuation. In addition, we measure and discuss the effect of the fold angle on the trigger and the hysteresis cycle width as part of the static losses. As adhesion forces are at the origin of a minimum energy cost required to move the film, regardless of the actuation speed, controlling them through surface engineering and the fold angle will be one of the main challenges in reducing static losses and actuation time, which are two key parameters for efficient thermal switches.

The experimental analysis and the modeling of the regimes observed when increasing voltage to speed up the actuation show that the main mechanism hindering high-voltage fast actuation is the appearance of surface charges related to the air ionization between the films. This allows pinpointing a key challenge that all electrostatic actuators will have to tackle.

For instance, the typical electrostatic thermal switches reported in the literature[4,5] are operating at up to 800 V. Our analysis shows that within such a high voltage range, the actuation efficiency is reduced by charges due to air ionization. Indeed, according to the results shown here, only a very wise optimization of the electrode surfaces, the air gap, and the control of the atmosphere within the device can make such high voltage accessible without reaching the Paschen threshold. Similarly, working with lower or higher pressure and gap (in relation to the Paschen law) may offer the opportunity to work on the left or right part of the Paschen curve, increasing the force, and avoiding the charge appearance.

Charge transfer resulting from air ionization above some voltage threshold and adhesive forces are ubiquitous in electrostatic actuators, but their influence varies depending on the geometry and the materials involved. While adhesion is expected to vary significantly across different film materials, the charge transfer associated with air remains largely consistent regardless of the material; however, more "leaky" dielectric materials—those with higher conductivity than Polypropylene (PP)—may introduce additional charge accumulation due to conduction[15].

Finally, in summary of the static losses of the EA, the trigger voltage is influenced by several factors, including film adhesion, the angle of the middle film, and the presence of charges related to the applied voltage and the EA speed.

CRediT authorship contribution statement

Elie Zoghbi: Conceptualization, Methodology, Investigation, Data curation, Formal analysis, Software, Validation, Visualization, Writing – original draft, Writing – review and editing. **Emilien Dufresne**: Conceptualization, Methodology, Investigation, Data curation, Formal analysis, Software, Validation, Visualization. **Martino LoBue**: Supervision, Project administration, Funding acquisition, Writing – review and editing. **Morgan Almanza**: Conceptualization, Methodology, Resources, Supervision, Project administration, Funding acquisition, Validation, Writing – review and editing.

Declaration of Competing Interest

The authors declare that they have no known competing financial interests or personal relationships that could have appeared to influence the work reported in this paper.

Acknowledgments

This research has received funding from the French National Research Agency (ANR) under the projects ECOOL (ANR-20-CE05-0044), CERACOOL (ANR-23-CE05-0012), and COOT (ANR-25-CE05-4167). It has also received financial support from the CNRS through the Accélération Ingénierie programme (project PerEC).

Appendix A. Supplementary data

Supplementary data to this article can be found online at doi: https://doi.org/10.1016/j.sna.2026.117709

Data availability

Data will be made available on request.

References

[1] N. Kellaris, V. Gopaluni Venkata, G. M. Smith, S. K. Mitchell, and C. Keplinger, "Peano-HASEL actuators: Muscle-mimetic, electrohydraulic transducers that linearly contract on activation," Science Robotics **3**, eaar3276 (2018).

[2] F. Pan, L. Chen, F. Liu, and X. Ji, "Electric field induced mechanical flapping motors enabling soft robotic and wearable applications," Sensors and Actuators A: Physical **376**, 115662 (2024).

[3] M. Almanza, L. Depreux, F. Parrain, and M. LoBue, "Electrostatically actuated thermal switch device for caloric film," **112**, 083901.

[4] R. Ma, Z. Zhang, K. Tong, D. Huber, R. Kornbluh, Y. S. Ju, and Q. Pei, "Highly efficient electrocaloric cooling with electrostatic actuation," Science **357**, 1130–1134 (2017).

[5] Y. Meng, Z. Zhang, H. Wu, R. Wu, J. Wu, H. Wang, and Q. Pei, "A cascade electrocaloric cooling device for large temperature lift," Nature Energy (2020), 10.1038/s41560-020-00715-3.

[6] Y. Bo, Q. Zhang, H. Cui, M. Wang, C. Zhang, W. He, X. Fan, Y. Lv, X. Fu, J. Liang, Y. Huang, R. Ma, and Y. Chen, "Electrostatic Actuating Double-Unit Electrocaloric Cooling Device with High Efficiency," Advanced Energy Materials , 2003771 (2021).

[7] J. Li, "Electrostatic Zipping Actuators and Their Application to MEMS," .

[8] W.-M. Zhang, H. Yan, Z.-K. Peng, and G. Meng, en"Electrostatic pull-in instability in MEMS/NEMS: A review," Sensors and Actuators A: Physical **214**, 187–218 (2014).

[9] L. Maffli, S. Rosset, and H. R. Shea, "Zipping dielectric elastomer actuators: characterization, design and modeling," **22**, 104013.

[10] L. Depreux, M. Almanza, N. Zeggai, F. Parrain, and M. LoBue, "Heat management and losses of electrocaloric cooling devices based on electrostatic thermal switches," Applied Thermal Engineering **211**, 118290 (2022).

[11] K. Sato and M. Shikida, "Electrostatic film actuator with a large vertical displacement," in *[1992] Proceedings IEEE Micro Electro Mechanical Systems* (IEEE, Travemunde, Germany, 1992) pp. 1–5.

[12] F. W. DelRio, M. P. de Boer, L. M. Phinney, C. J. Bourdon, and M. L. Dunn, "Van der Waals and Capillary Adhesion of Microelectromechanical Systems," in *Microelectromechanical Systems* (ASMEDC, Chicago, Illinois, USA, 2006) pp. 21–26.

[13] F. W. DelRio, M. L. Dunn, L. M. Phinney, C. J. Bourdon, and M. P. de Boer, "Rough surface adhesion in the presence of capillary condensation," Applied Physics Letters **90**, 163104 (2007).

[14] A. J. Kinloch, *Adhesion and Adhesives* (Springer Netherlands).

[15] I.-D. Sîrbu, D. Preninger, D. Danninger, L. Penkner, R. Schwödiauer, G. Moretti, N. Arnold, M. Fontana, and M. Kaltenbrunner, "Electrostatic actuators with constant force at low power loss using matched dielectrics," Nature Electronics **6**, 888–899 (2023).

[16] H. Zou, Y. Zhang, L. Guo, P. Wang, X. He, G. Dai, H. Zheng, C. Chen, A. C. Wang, C. Xu, and Z. L. Wang, "Quantifying the triboelectric series," **10**, 1427, publisher: Nature Publishing Group.

[17] H. Shea, A. Gasparyan, H. B. Chan, S. Arney, R. Frahm, D. Lopez, S. Jin, and R. McConnell, "Effects of electrical leakage currents on mems reliability and performance," IEEE Transactions on Device and Materials Reliability **4**, 198–207 (2004).

[18] W. A. de Groot, J. R. Webster, D. Felnhofer, and E. P. Gusev, "Review of device and reliability physics of dielectrics in electrostatically driven mems devices," IEEE Transactions on Device and Materials Reliability **9**, 190–202 (2009).

[19] S. E. Creager and T. T. Wooster, "A new way of using ac voltammetry to study redox kinetics in electroactive monolayers," Analytical Chemistry **70**, 4257–4263 (1998), https://doi.org/10.1021/ac980482l.

[20] K. Kendall, "Thin-film peeling-the elastic term," Journal of Physics D: Applied Physics **8**, 1449 (1975).

[21] K. Kendall and A. D. Roberts, "van der waals forces influencing adhesion of cells," 10.1098/rstb.2014.0078, publisher: The Royal Society.

[22] Y. I. Sobolev, W. Adamkiewicz, M. Siek, and B. A. Grzybowski, "Charge mosaics on contact-electrified dielectrics result from polarity-inverting discharges," **18**, 1347–1355.

[23] I. P. Raĭzer, *Gas Discharge Physics* (Springer, Berlin, 1997).

[24] M. A. Lieberman and A. J. Lichtenberg, *Principles of Plasma Discharges and Materials Processing*, 1st ed. (Wiley, 2005).

[25] J.-R. Riba and M. Soltany, "Modified paschen curves for non-uniform fields in air based on a rod–plane electrode geometry," Plasma Sources Science and Technology **34**, 125002 (2025).

[26] J.-M. Torres, M. Desmulliez, and R. Dhariwal, "Electric field breakdown at micrometre separations in air and nitrogen at atmospheric pressure," IEE Proceedings - Science, Measurement and Technology **147**, 261–265 (2000).

[27] A. Peschot, N. Bonifaci, O. Lesaint, C. Valadares, and C. Poulain, "Deviations from the paschen's law at short gap distances from 100 nm to 10 μm in air and nitrogen," Applied Physics Letters **105** (2014), 10.1063/1.4895630.